Fast and Robust Characterization of Lossy Dielectric Slabs Using Rectangular Waveguides

Xuchen Wang and Sergei A. Tretyakov, *Fellow, IEEE*

***Abstract*— Waveguide characterization of dielectric materials is a convenient and broadband approach for measuring dielectric constant. In conventional microwave measurements, material samples are usually mechanically shaped to fit waveguide opening and measured in closed waveguides. This method is not practical for millimeter-wave and sub-millimeter-wave measurements where waveguide openings become tiny, and it is rather difficult to shape the sample to exactly the same dimensions as the waveguide cross section. In this article, we present a method that allows one to measure arbitrarily shaped dielectric slabs that extend outside waveguides. In this method, the measured sample is placed between two waveguide flanges, creating a discontinuity. The measurement system is characterized as an equivalent Π-circuit, and the circuit elements of the Π-circuit are extracted from the scattering parameters. We have found that the equivalent shunt impedance of the measured sample is only determined by the material permittivity and is rather insensitive to the sample shape, position, sizes, and other structural details of the discontinuity. This feature can be leveraged for accurate measurements of permittivity. We provide an analytical extraction formula for thin-layer dielectric samples. For thick layers, a numerical optimization method based on a feed-forward neural network is introduced to retrieve the permittivity. The proposed method is very useful for measuring the permittivity of medium-loss and high-loss dielectrics from microwave to subterahertz frequencies.**

***Index Terms*— Deep learning, millimeter-wave, neural network, permittivity measurement, rectangular waveguide, submillimeter-wave.**

I. Introduction

MATERIAL characterization is an essential step in designing electromagnetic devices. The recent fast developments of wireless communications (5G and beyond) impose strong demands for the characterization of dielectric materials at millimeter-wave and even higher frequencies. In general, the methods for measuring dielectric constant can be divided into two groups: one is based on resonating systems and the other is using non-resonant transmission line structures [1]. In resonance-based methods, the sample is usually machined into a dielectric resonator with a high Q-factor. The real part of the permittivity can be predicted from the resonant frequency, and the loss tangent is extracted from the Q-factor of the measurement system, e.g. [2]–[4]. Alternatively, one can position the sample into a high-Q resonator and obtain the permittivity value by measuring the perturbation of the resonant frequency and the Q-factor of the system before and after loading the sample, e.g. [5]–[9]. Generally speaking, resonance methods provide the best accuracy in the estimation of both real and imaginary parts of permittivity for low-loss dielectrics. The drawback of the resonant methods is that the measured frequencies must be discrete, corresponding to the resonant frequencies of the system. In addition, the dimensions of the resonators become tiny at millimeter-wave or higher frequencies, which imposes considerable practical difficulties.

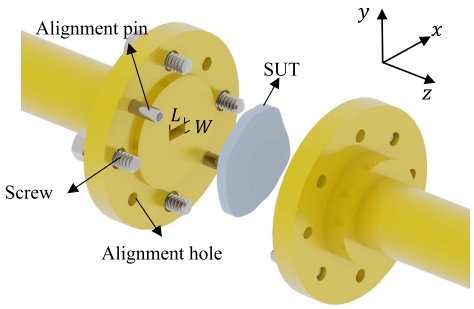

Fig. 1. Measurement setup using millimeter-wave rectangular waveguides. The SUT is positioned in between two waveguide flanges. The actual setup is fastened by screws.

In the transmission-line-based method, the measured sample is connected as a load or insertion in a waveguiding structure. By measuring the reflection and/or transmission coefficients (S-parameters) of the system, the dielectric properties of the material can be determined in a broad frequency range [10]. Due to the absence of a setup resonance, the measured S-parameters are not so sensitive to dielectric losses as in the resonator method (especially for thin dielectric samples), and therefore the measurement accuracy for loss tangent is generally worse than in the resonator method. For this reason, the transmission-line method is most suitable for characterization of medium-loss and high-loss dielectrics [1], [11]. Transmission-line structures can be formed by waveguide structures, such as metallic [12]–[14] or dielectric waveguides [2], [15], coplanar waveguides [16], and microstrip lines [17], where the wave is strictly confined and guided in the waveguides. Alternatively, free space can act as an unbounded waveguide [18], [19], but free-space measurements need large and controllable measurement space,

Manuscript received September 1, 2021; revised November 26, 2021; accepted January 3, 2022. Date of publication February 1, 2022; date of current version April 4, 2022. *(Corresponding author: Xuchen Wang.)*

The authors are with the Department of Electronics and Nanoengineering, Aalto University, 15500 Aalto, Finland (e-mail: xuchen.wang@aalto.fi).

Color versions of one or more figures in this article are available at https://doi.org/10.1109/TMTT.2022.3143827.

Digital Object Identifier 10.1109/TMTT.2022.3143827

large sample sizes, and accurate beam alignments. One of the most commonly used methods is developed in [12] and [13], which is well-known as the Nicolson–Ross–Weir method. In this method, the sample under test (SUT) is embedded into a rectangular waveguide and fully in contact with the waveguide walls. However, in practice, there are inevitable air gaps between the surfaces of the SUT and the waveguide walls. This is a considerable restriction for measurements at millimeter-wave and above frequencies where the waveguide dimensions are of the order of millimeter or smaller [20].

In order to avoid the problem of imperfect contact with the waveguide walls, it is preferable and easier to test the sample outside waveguides [21]–[24]. For example, in [22] and [23], the samples are positioned between two waveguide flanges, creating a discontinuity from which the electromagnetic energy is allowed to leak away. The measurement setup is then modeled in commercial simulation tools or using self-developed numerical algorithms to calculate the S-parameters. By fitting the numerically simulated S-parameters with the measured values, the permittivity of the sample can be estimated. However, in this method, it is necessary to ensure that the actual measurement setup is accurately represented in numerical modeling, e.g., the dimensions of the waveguide flanges and the test sample, since the S-parameters of the system are affected by all these details. Practical limitations on the modeling accuracy of all the setup details do not allow accurate millimeter-wave measurements, because the configuration of millimeter-wave waveguide flanges is usually not planar and contains other structures such as holes, chokes, alignment pins, and screws, which are difficult to model accurately (see Fig. 1). Obviously, in the millimeter-wave range and above, it is more convenient to measure the sample outside waveguides, without caring about the sample shape and positioning, the flange types, and other accessories.

In this article, we propose such a method that can be used to measure arbitrary-shaped dielectric slabs outside rectangular waveguides (see Fig. 1). We qualitatively analyze the electromagnetic fields in the discontinuity and use the understanding of field distribution to model the discontinuity as a Π-circuit where each circuit component can be extracted from the measured S-parameters. We have found that the equivalent shunt impedance of the discontinuity is rather insensitive to the sample shape and the structural details in the discontinuity, and it is only determined by the permittivity and thickness of the sample. This feature can be readily used for the extraction of dielectric permittivity if the sample thickness is known.

This article is organized as follows. In Section II, we introduce the physical principle of the proposed method. In Sections III and IV, we separately discuss the permittivity extraction methods for electrically thin and thick dielectric slabs. The measurement uncertainties are analyzed in Section V.

II. Measurement Principle

In this section, we introduce the physical principle of the proposed measurement method. We start from the field analysis for the measurement setup. Then, we model the discontinuity as an equivalent circuit and verify the stability of the equivalent shunt impedance.

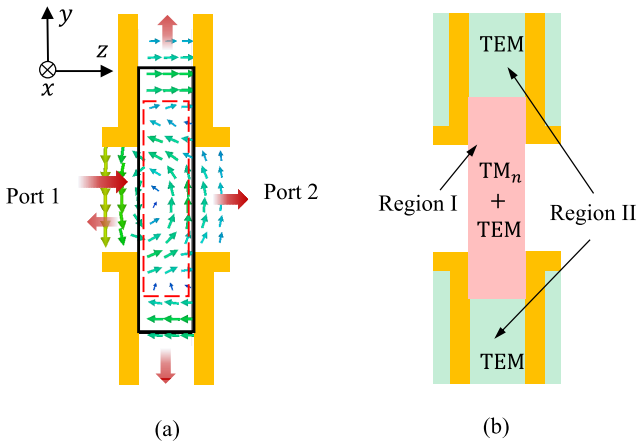

Fig. 2. (a) Vectorial field distribution in the yz cross section of the measurement setup for excitation from Port 1. In the simulations, the operating frequency is 60 GHz, the waveguide aperture size is $L = 3.76$ mm, and $W = 1.88$ mm (WR-15). Note that throughout this article, we use WR-15 waveguides for all the numerical and experimental analyses. The dielectric slab has a permittivity of $\epsilon_r = 4(1 - 0.01j)$ and thickness of $d = 625$ μm. (b) Division of regions. Note that the TEM and TM$_n$ modes correspond to PPWG, and not to the rectangular waveguide.

A. Field Distribution in the Discontinuity

Fig. 1 shows the actual measurement setup based on millimeter-wave-range rectangular waveguides. An arbitrarily shaped piece of a dielectric slab is positioned between two waveguide flanges. The waveguide aperture is fully covered by the dielectric sample. Although the structure of waveguide flanges contains many small details, for the following conceptual analysis it is possible to simplify the flanges as planar metallic walls. A cross section of the discontinuity is shown in Fig. 2(a). Waves incident from Port 1 are partially reflected and absorbed by the sample (shown as a black rectangle) and partially leak to free space via the gap. The rest of the power enters Port 2. The discontinuous junction is composed of a parallel-plate waveguide (PPWG) connected with a pair of rectangular waveguides. As we know, if the waveguides are continuous, and the operating frequency is below the cutoff frequencies of higher order modes, the rectangular waveguide only supports the TE$_{10}$ mode, and the PPWG only supports the TEM mode. However, in the junction, both rectangular waveguides and PPWG are discontinuous. To adapt to the configuration of the junction, higher order modes of the waveguides are excited. Therefore, the fields in the junction have a complicated composition, which is a combination of waveguide fundamental modes and many higher order modes. The field distribution in the junction region can be rigorously computed using the mode-matching method [22]. Fig. 2(a) shows the simulated electric field distribution in the waveguide junction. As we can see, near the rectangular waveguide apertures, strong TM$_n$ modes ($\mathbf{E}_y \neq 0$) of the PPWG are excited, and these modes continue to propagate in PPWG along the y-direction. However, after the higher order modes

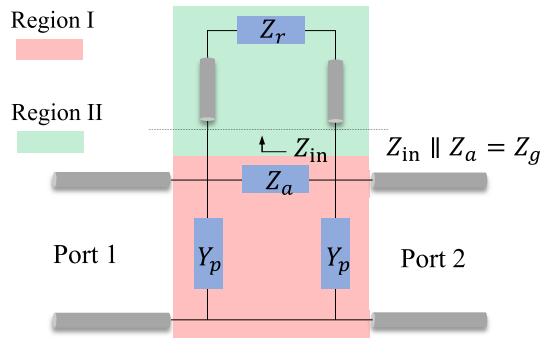

Fig. 3. Equivalent circuit of the measurement setup.

leave the junction region, they only see a continuous PPWG. Since the excitation frequency is below the cutoff frequencies of these higher order modes in the PPWG, these modes are evanescent and decay exponentially away from the junction. At some distance (see the top/bottom edge of the red dashed rectangle), the higher order modes become negligible and only the fundamental TEM mode continues propagation in PPWG formed by two flanges.

B. Circuit Modeling of the Discontinuity

According to the field distribution in Fig. 2(a), the electromagnetic environment of the discontinuity can be divided into two volumetric regions [see Fig. 2(b)]: Region I (highlighted in pink) encloses the volume where TM_n modes survive; Region II (highlighted in green) includes the remaining volume and all the surroundings outside the setup. Region I ($\mathbf{E}_y \neq 0$) is directly connected to the waveguide ports, and therefore it can be viewed as a two-port system.

Any passive two-port electromagnetic system can be modeled by an equivalent Π-circuit. We model Region I as a Π-circuit formed by two parallel admittances Y_p (these two admittances are identical due to the structural symmetry) and one series impedance Z_a, as shown in Fig. 3. For electrically thin gaps, the shunt admittance is capacitive (as will be numerically confirmed in the next section), because the vertical electrical field of TM_n modes, $\mathbf{E}_y$, represents the capacitive coupling between the top and bottom edges of the waveguide apertures. Region II ($\mathbf{E}_y = 0$) is an open-ended parallel-plate waveguide, which can be considered as a section of a transmission line terminated with an effective load impedance Z_r as a model of the open end (Z_r includes edge reactance and the radiation resistance of the open end of PPWG). The input impedance of Region II (seen from Region I) is denoted as Z_{in} which is a shunt connected to Z_a, as shown in Fig. 3. From Fig. 3, it is obvious that the whole gap (including Regions I and II) can be characterized as a unified Π-circuit, where the two shunt admittances Y_p are inherited from Region I and the series impedance Z_g is formed by a parallel connection of Z_{in} and Z_a, denoted as $Z_g = Z_a \parallel Z_{\text{in}}$.

If the sample size is larger than Region I, modifications of the sample shape change the electromagnetic environment in Region II and thus influence Z_{in}. Moreover, for millimeter and sub-terahertz waveguides, the flange walls are normally not planar. Any additional passive structures in Region II, e.g., fastening screws, choke grooves, tapped holes, and alignment pins, can be viewed as additional loadings of PPWG, and thus they also affect the value of Z_{in}. As a consequence, the total series impedance may significantly vary when the shape and size of the dielectric sample are changed. Even different positioning of the same sample or different tightness of fastening affects the series impedance. However, the shunt impedance of the discontinuity will not be affected by these structural details in Region II, since it is only determined by the capacitive coupling of the waveguide walls in Region I which is very stable once the sample area is larger than Region I. For this reason, we can leverage the stable shunt impedance to characterize slab samples with arbitrary shapes positioned between arbitrary flanges. Note that the stability of shunt impedance was noted in our previous work [25], but at that time, we did not realize that it can be used for permittivity extraction.

C. Stability of the Shunt Impedance

In the equivalent circuit of Fig. 3, the values of Z_g and Y_p can be extracted from the measured S-parameters. We use the transfer matrix method. After expressing the circuit components Y_p and Z_g in terms of $ABCD$ matrices, the total transfer matrix of the discontinuity can be calculated as the cascaded multiplication of them

$$\begin{bmatrix} A & B \\ C & D \end{bmatrix} = \begin{bmatrix} 1 & 0 \\ Y_p & 1 \end{bmatrix} \begin{bmatrix} 1 & Z_g \\ 0 & 1 \end{bmatrix} \begin{bmatrix} 1 & 0 \\ Y_p & 1 \end{bmatrix} = \begin{bmatrix} 1 + Z_g Y_p & Z_g \\ Z_g Y_p^2 + 2Y_p & 1 + Z_g Y_p \end{bmatrix}. \tag{1}$$

The matrix elements, A, B, C, and D, can be expressed as functions of S-parameters [26, § 4.4]. Therefore, we can relate the circuit values with S-parameters. Parameter Z_g can be expressed as

$$Z_g = B = Z_0 \frac{(1 + S_{11})^2 - S_{21}^2}{2S_{21}}. \tag{2}$$

Here, $Z_0 = \omega\mu_0/\sqrt{\omega^2\mu_0\epsilon_0 - (\pi/L)^2}$ is the characteristic impedance of the TE_{10} mode in the rectangular waveguide. Another equation can be written as

$$1 + Z_g Y_p = A = \frac{1 - S_{11}^2 + S_{21}^2}{2S_{21}}. \tag{3}$$

Solving Y_p from (2) and (3), we obtain

$$Y_p = \frac{A - 1}{Z_g} = \frac{1 - S_{11} - S_{21}}{Z_0(1 + S_{11} + S_{21})}. \tag{4}$$

Next, we numerically demonstrate that Y_p is insensitive to the shape of the sample and to possible additional structures inside the waveguide discontinuity. In the simulations, the values of the permittivity and the thickness of the dielectric slab are the same as assumed in Fig. 2(a). The measurement setup is modeled in three different ways. In the first case, the sample covers the waveguide aperture with dimension $W \times L$ and extends to the distance Δs from the aperture edges, as illustrated in the first inset picture of Fig. 4 (top).

We increase the extended size Δs and extract the shunt impedance $Z_p = 1/Y_p$ and series impedance Z_g from the simulated S_{21} and S_{11} according to (2) and (4). It can be seen that as Δs increases, the shunt impedance remains constant, while the series impedance is very unstable. This is because the changes in the dielectric sample sizes modify the input impedance of Region II and thus change Z_g dramatically. Note that when the sample size is close to the waveguide aperture ($\Delta s \approx 0$), the extracted shunt impedance becomes sensitive to size variations. This is because in this case the dominating TM_1 mode does not fully decay in the sample, and the variations in the sample size affect the field distribution in Region I and therefore change the shunt impedance. Obviously, there exists a critical extension size $\Delta s_{\rm cr}$, for which the amplitude of the TM_1 mode decays to $e^{-\alpha}$ (α is the decaying factor which is enough large) of the originally excited amplitude when it propagates in PPWG. According to this criterion, $\Delta s_{\rm cr}$ can be calculated as

$$\Delta s_{\rm cr} = \frac{\alpha}{\sqrt{(\frac{\pi}{d})^2 - \omega^2 \epsilon_{\rm r} \epsilon_0 \mu_0}}. \tag{5}$$

Therefore, the size of the test slab should be larger than $(L + 2\Delta s_{\rm cr}) \times (W + 2\Delta s_{\rm cr})$ to ensure that the higher order modes are negligible at the edges of the sample. The critical extension size for Case I in Fig. 4 is $\Delta s_{\rm cr} = 0.69$ mm for $\alpha = 3$. As we can see from Fig. 4 (top), the shunt impedance of the gap does not change when $\Delta s > \Delta s_{\rm cr}$.

In Case II, we choose an arbitrarily shaped dielectric slab that is larger than the critical size. It is shown that the shunt impedance still keeps unchanged. In Case III, the waveguide flanges are modified into a circular shape with actual screws, alignment pins, and choke grooves. We see that even with such a complicated gap environment, the shunt impedance Y_p is still not affected at all.

The above numerical experiments fully verify the predictions based on circuit modeling, confirming that the shunt impedance of the gap is insensitive to the gap environment and to the shape and size of the sample. In the next section, we will show how to extract the permittivity from the measured Y_p.

III. Characterization of Electrically Thin Dielectric Slabs

Next, we discuss how Y_p is related to the permittivity of the dielectric slab under test. Unlike the conventional waveguide characterization, here, the S-parameters have no explicit analytical relationships with ϵ_r. Therefore, it is not straightforward to find the permittivity from the measured S-parameters and the shunt admittance Y_p. In this section, we discuss the extraction methods for electrically thin dielectric layers ($d < \lambda_d/10$, where $\lambda_d = \lambda_0/\mathrm{Re}(\sqrt{\epsilon_r})$ is the wavelength in the material), derive the extraction formulas, and show the measurement results.

A. Extraction Formula

For samples with ultra-subwavelength electrical thickness ($d < \lambda_d/10$), the fields in Region I are similar to the field in a material slab placed in a continuous rectangular waveguide. This is because very thin flange gaps have very large parallel-plate capacitances, allowing the currents on the metal walls of the waveguides to pass through the gap. Therefore, the shunt impedance of Region I can be approximated considering the same dielectric slab in a closed waveguide. To find the shunt impedance of a dielectric slab inside the waveguide, a convenient way is to use the corresponding $ABCD$ matrix. By equating the matrix elements with that in (1), we can solve all the circuit components (Y_p and Z_g). The $ABCD$ matrix of a dielectric slab inside a continuous waveguide can be expressed as

$$\begin{bmatrix} A & B \\ C & D \end{bmatrix} = \begin{bmatrix} \cos(\beta_d d) & jZ_d \sin(\beta_d d) \\ jY_d \sin(\beta_d d) & \cos(\beta_d d) \end{bmatrix} \tag{6}$$

where $\beta_d = \sqrt{\omega^2 \mu_0 \epsilon_0 \epsilon_r - (\pi/L)^2}$ is the propagation constant in the dielectric slab (TE_{10} mode), and $Z_d = \mu_0 \omega / \beta_d$ is the corresponding characteristic impedance. After equating the matrix elements in (6) and (1), Y_p can be analytically solved

$$Y_p = \frac{\cos(\beta_d d) - 1}{jZ_d \sin(\beta_d d)} = \frac{1 - S_{11} - S_{21}}{Z_0(1 + S_{11} + S_{21})}. \tag{7}$$

Once the S-parameters are measured, the above equation uniquely determines ϵ_r [note that in (7), β_d is a function of ϵ_r].

To examine the accuracy of extraction formula (7), let us consider a dielectric slab with $d = 100$ μm and $\epsilon_r = \epsilon_r' - j\epsilon_r'' = 4 - j0.04$. The electrical thickness is $d = \lambda_d/25$ at 60 GHz. We simulate the setup with these assumed physical parameters and obtain the S-parameters from 50 to 75 GHz. Using (7), we solve the complex permittivity at each frequency point. The results are shown in Fig. 5. The retrieved permittivity perfectly agrees with the value assumed in the simulation.

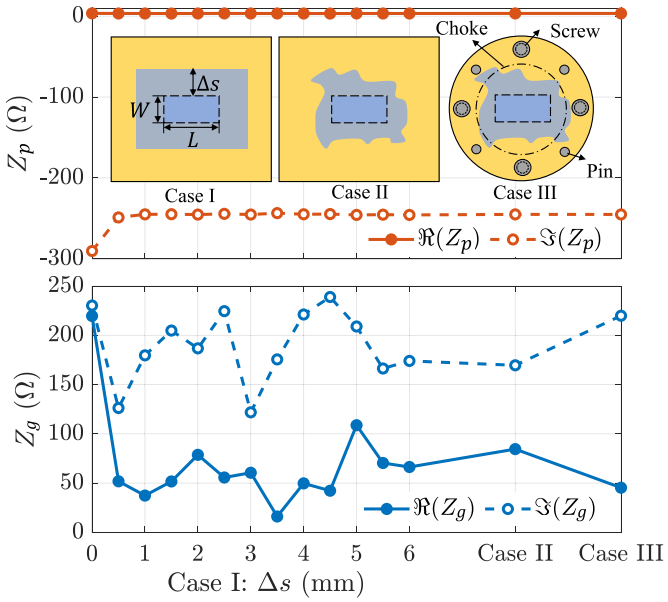

Fig. 4. Extracted shunt (top) and series (bottom) impedances for different sample dimensions. In Case I, the sample size is $(L + 2\Delta s) \times (W + 2\Delta s)$. In Case II, the sample shape is randomly chosen but it is larger than the critical size. In Case III, the waveguide flanges are round with small accessory structures.

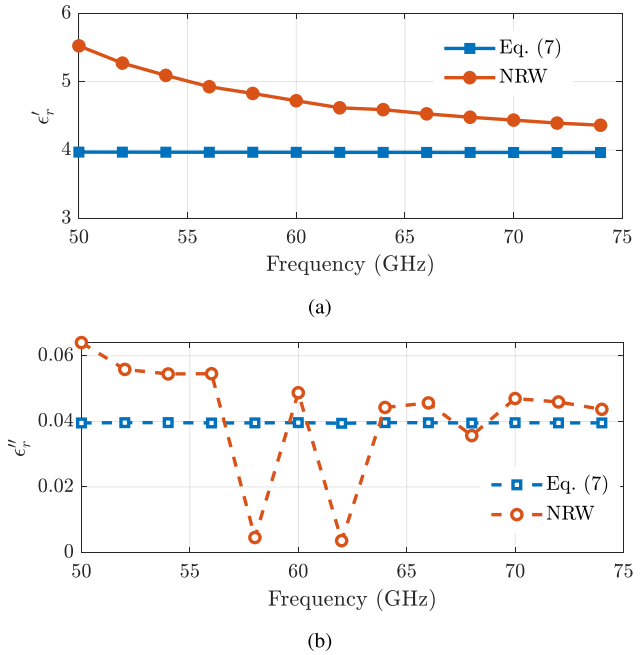

Fig. 5. (a) Real and (b) imaginary (bottom) parts of permittivity solved from (7) and using Nicolson–Ross–Weir (NRW) method. In the simulation setup, the sample is rectangular shaped with $\Delta_s = 1$ mm. Note that throughout this article, the complex permittivity is defined using engineering convention, i.e., $\epsilon_r = \epsilon_r' - j\epsilon_r''$.

It should be noted that although for thin slabs only a very small amount of power leaks away from the discontinuity, one cannot ignore it and use the conventional Nicolson–Ross–Weir formulas (which are derived for closed waveguides) to extract the permittivity. In Fig. 5, the extraction results using (7) and the Nicolson-Ross–Weir formulas [12] are compared. We see that even for such a thin gap, the Nicolson-Ross–Weir method does not work due to the negligence of leaked power. The proposed method is, however, fully applicable, because it extracts the permittivity via the shunt impedance, but not directly from the S-parameters.

It is important to stress that the permittivity extraction formula (7) is only accurate for ultra-thin dielectric materials, i.e., when $|\beta_d|d \ll 1$. Under this condition, we can make the following additional approximations in (7): $\cos(\beta_d d) - 1 \to -(\beta_d d)^2/2$ and $\sin(\beta_d d) \to \beta_d d$ and obtain

$$Y_p \approx \frac{j}{2}\left(\omega\epsilon_0\epsilon_r - \frac{\pi^2}{\omega\mu_0 L^2}\right)d. \tag{8}$$

Equation (8) implies that at a fixed frequency, $\Re(Y_p)$ and $\Im(Y_p)$ are linearly dependent on ϵ_r'' and ϵ_r', respectively. Note that since (8) is derived from (7) with some approximations, we will not use it to extract the permittivity. All the extraction results in Section III are obtained by numerically solving (7).

B. Measurement Results

The extraction formula (7) is suitable for thin-film characterization at microwave and millimeter-wave frequencies, e.g., polyethylene naphthalate (PEN) and polyethylene terephthalate (PET) films with the thickness around 100 μm which is much smaller than the wavelength. Conservative thickness range for using (7) is below $\lambda_d/10$ at the center measurement frequency. It is important to mention that measuring extremely thin sheets (several tens of microns) requires more accurate mechanical assembling of the setup (especially, alignment and fastening of the two flanges) to ensure full contact between the sample and flanges. Misalignment or unbalanced screwing will create an air gap between the sample and flanges and therefore change the effective thickness of the sample. To avoid this problem, one can stack several layers of thin films to increase the total thickness of the measured sample (still keeping it below $\lambda_d/10$), reducing the effects of possible misalignments.

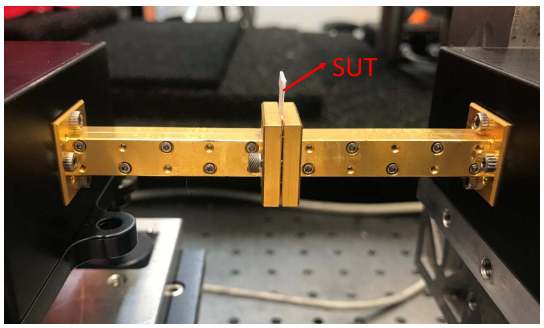

Fig. 6. Photograph of the measurement setup. In this example, the SUT is four layers of stacked copy papers. The waveguides are connected to WR-15 vector network analyzer extender (black modules).

Here, we measure the permittivity of common copy paper and experimentally show the stability of shunt impedance. We stack four layers of 80-μm-thick STAPLES copy paper, forming a 320-μm-thick sample ($d = \lambda_d/10$ at 60 GHz). The sample is cut into an arbitrary shape but larger than $(L + 2\Delta s_{\rm cr}) \times (W + 2\Delta s_{\rm cr})$ to ensure the stability of shunt impedance. The measurement comprises several steps.

1) Calibrate the system using thru-reflect-line (TRL) method.
2) Embed the sample between the flanges (see Fig. 6). Note that it is not necessary to use a sample holder. One can cut the sample into a long strip that covers the waveguide aperture and hold it by hand when connecting the waveguides. After the sample is placed, close the waveguides and fasten the flanges using screws.
3) Measure the S-parameters of the setup. At this step, proper time gating can be applied to filter parasitic reflections caused by waveguide misalignments. One should be careful not to remove harmless reflections from the sample edge and other structures inside the flanges; otherwise, the extraction results will instead become less accurate.
4) Record the S-parameters and use (7) to numerically extract the permittivity.

Fig. 7 shows the measured magnitudes of S-parameters for two samples cut in arbitrarily different shapes. One can see that the measured S-parameters are obviously not the same for the two samples, since the sample shapes and sizes in Region II are different. The difference in the measured S-parameters will pass on to the extracted series impedance, which is different

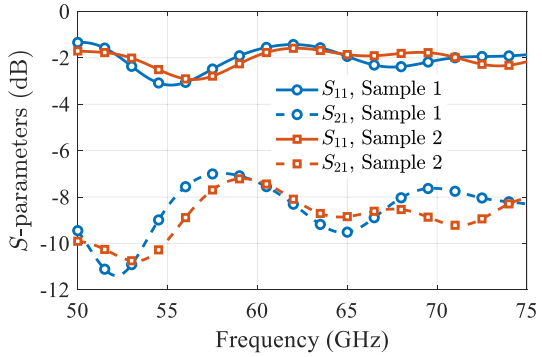

Fig. 7. Measured S-parameters of two paper samples of different shapes.

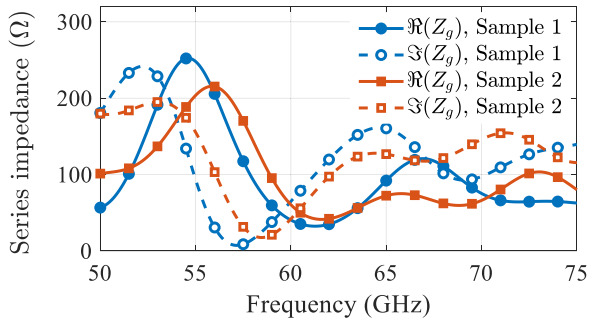

(a)

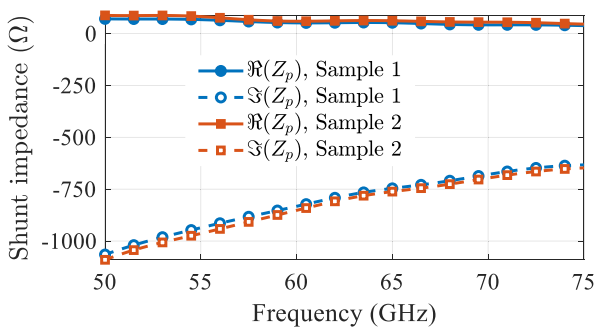

(b)

Fig. 8. Extracted (a) series and (b) shunt impedances of the discontinuity created by two different samples.

for different samples, as shown in Fig. 8(a). In contrast, the measured shunt impedance is very stable, as shown in Fig. 8(b).

The extracted complex permittivity [using (7)] of two paper samples is shown in Fig. 9. The results for the two samples are very close and stable in the studied frequency ranges, also agreeing with previously reported results [27]. The slight difference might result from different actual thickness of the paper samples caused by different tightness of the screws.

To further verify the accuracy of the method, we measure the permittivity of PEN layers and, as a further validation check, of free space. PEN samples are stacked in two layers (the thickness of each layer is 125 μm), and the total thickness is about $d \approx \lambda_d/12$ at 60 GHz. The extracted permittivity is shown in yellow curves in Fig. 9. The measured value is

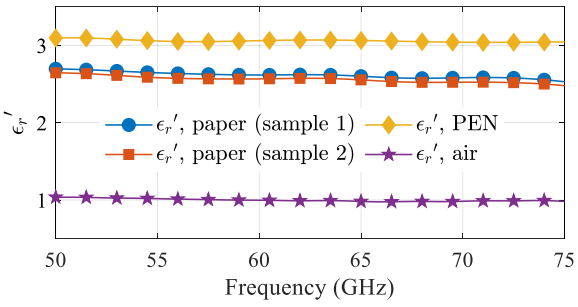

(a)

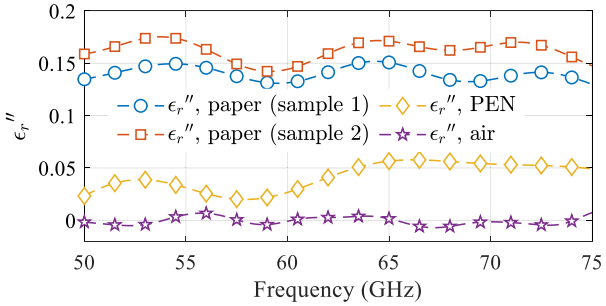

(b)

Fig. 9. Extracted (a) real and (b) imaginary parts of permittivity for different types of materials.

around $\epsilon_r = 3.05 - j0.05$, being in good agreement with the previously reported values in [28] and [29] at millimeter-wave frequencies. We also measure the permittivity of air. The "air sample" is formed by opening an arbitrary-shaped (but larger than the critical size) hole in a 400-μm-thick FR4 laminates. The extraction results are shown in Fig. 9 (purple curves), confirming good accuracy. In all the measured samples, it appears that the imaginary part of permittivity suffers more perturbations than the real part. This is caused by uncertainties of the measured S-parameters. The reason will be explained in Section V where the measurement uncertainties for both the real and imaginary parts of permittivity are analyzed in detail.

Importantly, one should remember that the extraction formula (7) is only accurate for electrically thin material layers ($d < \lambda_d/10$). As the electrical thickness of SUT increases, the extraction formula gradually becomes less accurate.

IV. Characterization of Thick Dielectric Layers

When the thickness of dielectric slabs increases ($\lambda_d/10 < d < \lambda_d/2$), the higher order TM modes become more and more significant in Region I, and the field in Region I can be obviously different from the field in the closed waveguide. Therefore, one cannot use a simple transmission-line section model for Region I, and the extraction formula (7) becomes inaccurate. Obviously, the relationship between Y_p and ϵ_r is not as straightforward as for thin samples.

A. Simulation-Assisted Extraction Method

Here, we use numerical tools (Ansys HFSS), to find the relationship between Y_p and ϵ_r. Numerical fitting is a

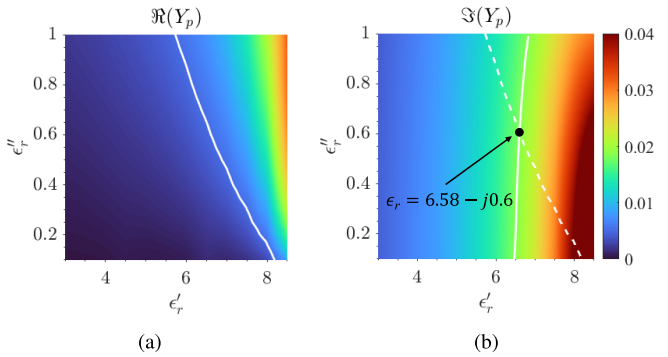

Fig. 10. (a) Real and (b) imaginary parts of shunt admittance at 75 GHz in terms of real and imaginary parts of permittivity. The data are obtained from numerical simulation using HFSS.

common method to extract material parameters from measured data. By modeling the measurement setup in numerical tools and fitting the simulated S-parameters with the measured values, one can estimate the permittivity of the sample. In the conventional numerical fitting method, one should accurately model the actual measurement setup [15] since the modeling errors can induce significant inaccuracy in the simulated S-parameters and thus result in erroneous estimations of permittivity. To overcome this problem, instead of fitting the scattering parameters, we fit the equivalent shunt impedance/admittance. As we demonstrated in Section II-C, the shunt impedance/admittance is only related to the thickness (which is easy to measure) and the sample permittivity, and it is not affected by the details of the discontinuity and external environment. In this way, one can avoid the need to accurately reproduce all the setup details in simulation tools. The measurement procedure compromises the following steps.

1) The sample is measured in a waveguide junction. The shunt admittance is extracted from the measured S-parameters using (4).
2) The physical setup is modeled in the simulation tool. Note that it is not necessary to accurately model the measurement setup in the simulation since the complicated structures of the waveguide junction and the shape of the sample (as long as it is larger than the critical size) do not affect the shunt admittance.
3) At the frequencies of interest, different values of permittivity (both real and imaginary parts) are assumed in the simulation, and the shunt admittance is extracted from numerical results. The simulated shunt impedance is then compared with the measured values. When the simulated and measured values are identical, the permittivity assumed in the simulation is the actual permittivity of the material under test.

For example, we assume the thickness of SUT is $d = 660\ \mu$m and the frequency of interest is $f = 75$ GHz. We model the measurement setup in HFSS and vary ϵ_r' and ϵ_r'' within reasonable ranges. For each pair of ϵ_r' and ϵ_r'', we can calculate the corresponding shunt admittance using (4). In this way, we can plot $\Re(Y_p)$ and $\Im(Y_p)$ as functions of ϵ_r' and ϵ_r'', as shown in Fig. 10. Let us assume the measured shunt admittance at 75 GHz is $Y_p = 0.005 + j0.018$. Then, we draw two contour curves $\Re(Y_p) = 0.005$ and $\Im(Y_p) = 0.018$ in Fig. 10(a) and (b) (white solid curves), respectively. The intersection point of the two contour curves ($\epsilon_r = 6.58 - j0.6$) in Fig. 10(b) is the measured value of permittivity at 75 GHz.

B. Measurement Results

In this section, we measure the permittivity of a mobile phone screen glass (Corning Gorilla Glass 6) with a thickness $d = 660\ \mu$m. The shunt admittance is extracted from the measured S-parameters, as shown in Fig. 12(a). To extract the permittivity at all measured frequencies, it is not efficient to fit the permittivity value at each frequency one by one, following the procedure introduced at the end of Section IV-A. Here, we use a deep learning technique to analyze the simulation data and quickly extract the permittivity at all the frequencies of interest.

In numerical simulations, we model the setup and perform parametric studies in terms of f, ϵ_r', and ϵ_r''. From simulations, we obtain more than 2000 sets of data, $[f, \epsilon_r', \epsilon_r'', \Re(Y_p), \Im(Y_p)]_{\text{simu}}$. The task is to use the simulated dataset to find ϵ_r' and ϵ_r'' for a given set of $[f, \Re(Y_p), \Im(Y_p)]_{\text{meas}}$ that is obtained from measurements. This is a multi-dimensional fitting problem. We use the neural net fitting app in MATLAB to train a fitting network. A feed-forward neural network was chosen to train the data. Fig. 11 illustrates the architecture of the network that contains three fully connected layers: an input layer with three nodes (corresponding to the input parameters f, $\Re(Y_p)$, and $\Im(Y_p)$), one hidden layer with ten nodes, and an output layer with two nodes (corresponding to ϵ_r' and ϵ_r''). In the model training, the input datasets are $[f, \Re(Y_p), \Im(Y_p)]_{\text{simu}}$ and the output datasets are $[\epsilon_r', \epsilon_r'']_{\text{simu}}$. The datasets are divided into three groups: 70% for training, 15% for validation, and 15% for testing. The Levenberg–Marquardt Algorithm is chosen to update the weight ($\mathbf{W_1}$, $\mathbf{W_2}$) and bias ($\mathbf{b_1}$, $\mathbf{b_2}$) values in each iteration until the trained model can accurately map the input and output datasets. With this algorithm, the training can be completed within several seconds. Once the fitting model is trained, the measured datasets $[f, \Re(Y_p), \Im(Y_p)]_{\text{meas}}$ are fed to the model as inputs, and the model can automatically output the predicted permittivity.

Fig. 12(b) shows the extracted permittivity in the measured frequency range. The real part of permittivity is between 6.6 and 6.8, which is in good agreement with the reference value ($\epsilon_r = 6.69 - j0.087$ at $f = 3$ GHz, measured in [30]). At millimeter-wave frequencies, the material loss (the measured values $0.4 < \epsilon_r'' < 0.66$ over this frequency range) significantly increases when compared with the provided value at microwave frequencies.

V. Uncertainty Analysis

The measurement uncertainty originates from inaccuracies in the measurement of sample thickness, flanges' alignments, imperfect contact between SUT and flange walls, and so on. The measurement errors caused by those factors can be reduced using high-precision thickness characterization

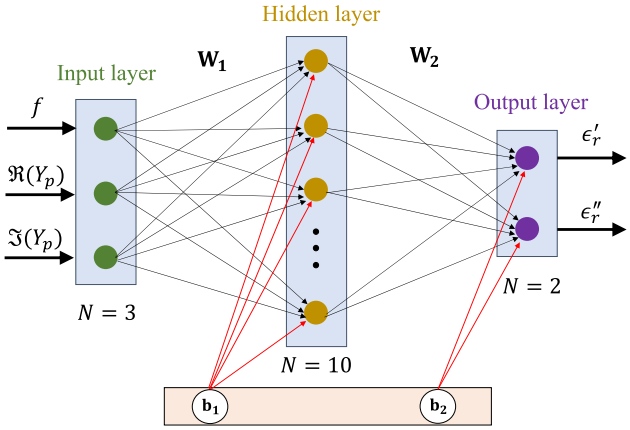

Fig. 11. Schematic of the feed-forward neural network.

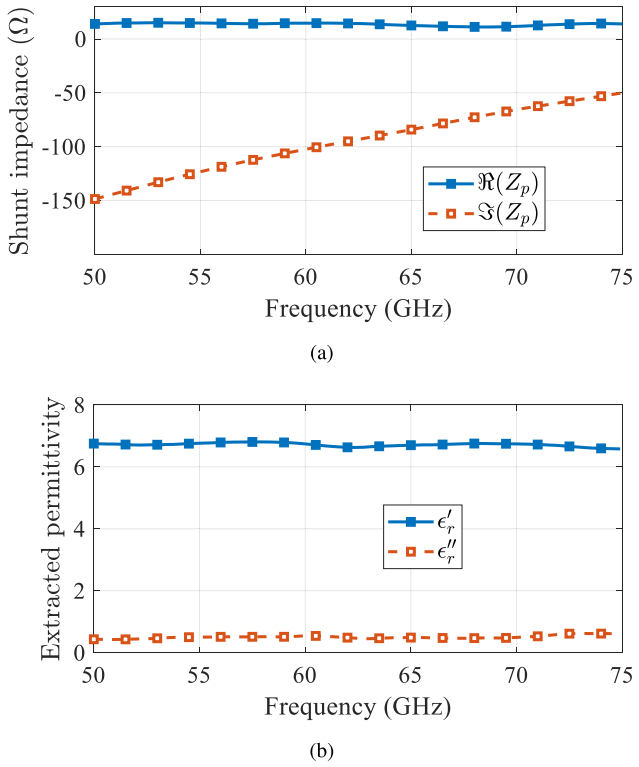

Fig. 12. Measured (a) shunt impedance and (b) permittivity of Corning Gorilla Glass 6 used for screens of mobile devices.

devices (e.g., profilometers) and careful assembling of the measurement setup. Other important sources of measurement errors include uncertainties of the measured S-parameters (both magnitude and phase), which are unavoidable and determined by VNA device parameters.

In this section, we study the measurement errors caused by uncertainties of the measured S-parameters. The uncertainties of the S-parameters on both magnitude and phases are denoted as $|\Delta S_\alpha|$ and $\Delta\theta_\alpha$ ($\alpha = 11, 21$), respectively. To analyze the impact of these parameters on the extracted permittivity, we use the differential method, where the dependent variable, ϵ_r, is differentiated with respect to each possible error parameter (the magnitudes and phases of the S-parameters

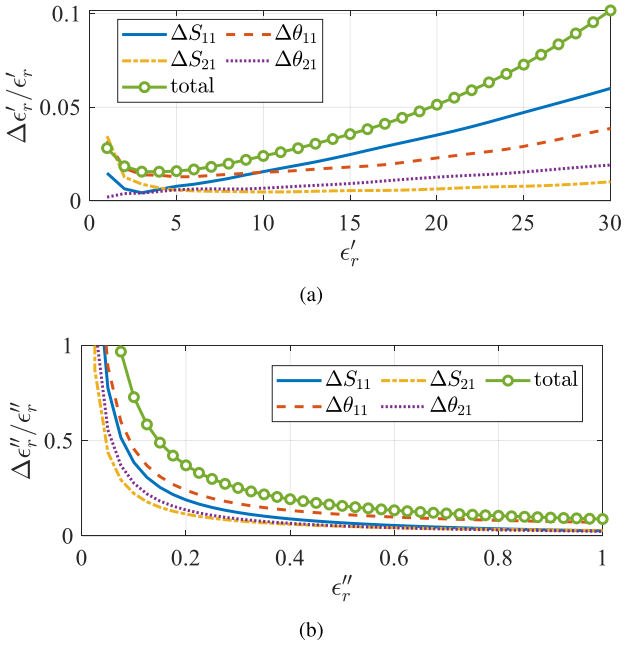

Fig. 13. Measurement uncertainties for (a) real and (b) imaginary parts of permittivity caused by each error source ($|\Delta S_\alpha|$ and $\Delta\theta_\alpha$) and their total effects.

involved in the extraction method) [25], [31]. Since each derivative can take positive or negative values, the final error is calculated as a sum of the squared values of all derivatives

$$\Delta\epsilon_r = \sqrt{\sum_\alpha \left(\frac{\partial\epsilon_r}{\partial|S_\alpha|}\Delta|S_\alpha|\right)^2 + \sum_\alpha \left(\frac{\partial\epsilon_r}{\partial\theta_\alpha}\Delta\theta_\alpha\right)^2} \tag{9}$$

where

$$\frac{\partial\epsilon_r}{\partial|S_\alpha|} = \frac{\partial\epsilon_r}{\partial Y_p}\frac{\partial Y_p}{\partial|S_\alpha|}, \quad \frac{\partial\epsilon_r}{\partial\theta_\alpha} = \frac{\partial\epsilon_r}{\partial Y_p}\frac{\partial Y_p}{\partial\theta_\alpha}. \tag{10}$$

In (10)

$$\frac{\partial Y_p}{\partial|S_\alpha|} = \frac{-2}{Z_0F^2}\frac{S_\alpha}{|S_\alpha|}, \quad \frac{\partial Y_p}{\partial\theta_\alpha} = \frac{-2j}{Z_0F^2}S_\alpha \tag{11}$$

with $F = 1 + S_{11} + S_{21}$. Furthermore, in (10), $\partial\epsilon_r/\partial Y_p = 2/(j\omega\epsilon_0 d)$ according to (8) for thin dielectric samples. For a thick layer, the linear dependence of Y_p on ϵ_r does not hold, as seen from Fig. 10. Therefore, numerical fitting techniques, e.g., "lsqnonlin" function in MATLAB, are needed to model the nonlinear relationship between ϵ_r and Y_p.

Let us assume that the sample thickness is $d = 280$ μm and the testing frequency is $f = 60$ GHz. In the first analysis, we evaluate the uncertainty of the real part of permittivity. To do this, we fix $\tan\delta = 0.01$ and sweep ϵ_r' from $\epsilon_r' = 1$ to $\epsilon_r' = 30$ in simulation and obtain the corresponding S_α for each permittivity value. In real measurements, the uncertainties of $|\Delta S_\alpha|$ and $\Delta\theta_\alpha$ depend on the magnitude of S_α, and the dependence can be obtained from Keysight Uncertainty Calculator for a specific vector analyzer [32]. In this work, we choose E8361C Vector Network Analyser with V11644A Calibration Kit in the calculator. Therefore, for each set of ϵ_r'

and ϵ_r'', we can calculate the uncertainties of $\Delta\epsilon_r'$ and $\Delta\epsilon_r''$ using (9), where $\partial\epsilon_r/\partial|S_\alpha|$ and $\partial\epsilon_r/\partial\theta_\alpha$ are obtained from the simulation, and, ΔS_α and $\Delta\theta_\alpha$ are provided by the VNA manufacturer.

The uncertainty of ϵ_r' is plotted in Fig. 13(a). It can be seen that the measurement uncertainty remains relatively low (below 5%) for ϵ_r' ranging from $\epsilon_r' = 1$ to $\epsilon_r' = 20$. The uncertainty reaches its minimum (1.5%) for $\epsilon_r' \approx 4$. For larger ϵ_r', $\Delta\epsilon_r'$ increases. This is because as the slab becomes more reflective, the uncertainty of $|S_{11}|$ increases as its magnitude increases, which results in a decrease in measurement accuracy.

In the second example analysis, the uncertainty of the imaginary permittivity is evaluated. In this case, we fix $\epsilon_r' = 5$ and vary ϵ_r'' from $\epsilon_r'' = 0$ to $\epsilon_r'' = 1$ in simulations. We can see in Fig. 13(b) that for high-loss dielectrics, the measurement errors of ϵ_r'' are small. However, for low-loss dielectrics, the relative uncertainty significantly increases. This is because when the wave goes through a low-loss dielectric slab, the attenuation cannot be sufficiently accumulated, and the changes in S-parameters caused by material losses are not evident. In this case, uncertainties in S-parameters can easily cause inaccurate estimations of the loss tangent. This is the common shortcoming of the transmission/reflection method for measuring thin low-loss material samples [31]. For lossy dielectrics, the influences of material loss on the measured S-parameters are observable, and the imaginary part of permittivity can be estimated accurately.

Finally, we should note that the S-parameter uncertainties provided by the VNA manufacturer are their worst values. In reality, the perturbations of S-parameters are not so strong, and the uncertainties shown in Fig. 13 might be overestimated. Good evidence is Fig. 9(b) where the extracted imaginary part of permittivity does not fluctuate as strongly as estimated.

VI. Conclusion

To summarize, this article reports a fast and robust method to measure dielectric slabs in a rectangular waveguide junction. The method does not require meticulous control of sample shape and position, which is particularly useful for millimeter-wave and sub-terahertz-wave measurements. The physics behind this method is that the equivalent shunt impedance of the waveguide junction is only related to the permittivity of the measured material if the thickness of the sample is known in advance. We develop an analytical formula to extract the permittivity of electrically thin materials ($d < \lambda_d/10$). For thick dielectrics ($\lambda_d/10 < d < \lambda_d/2$), the extraction formula becomes inaccurate, and in this case, numerical tools (HFSS combined with deep learning networks) are needed to extract the permittivity. The method can accurately retrieve the real part of permittivity, while the prediction of the imaginary part is accurate only for medium-loss and high-loss materials. It should be noted that the proposed method is only suitable for non-magnetic materials. For magnetic materials (both $\epsilon_r \neq 1$ and $\mu_r \neq 1$), the method is not able to retrieve both the permittivity and permeability.

Acknowledgment

The authors would like to thank F. Cuesta for help in glass sample measurements.

References

[1] J. Krupka, "Frequency domain complex permittivity measurements at microwave frequencies," *Meas. Sci. Technol.*, vol. 17, no. 6, pp. R55–R70, Jun. 2006.

[2] K. Z. Rajab, K. F. Fuh, R. Mittra, and M. Lanagan, "Dielectric property measurement using a resonant nonradiative dielectric waveguide structure," *IEEE Microw. Wireless Compon. Lett.*, vol. 15, no. 2, pp. 104–106, Feb. 2005.

[3] J. Krupka, K. Derzakowski, A. Abramowicz, M. E. Tobar, and R. G. Geyer, "Use of whispering-gallery modes for complex permittivity determinations of ultra-low-loss dielectric materials," *IEEE Trans. Microw. Theory Techn.*, vol. 47, no. 6, pp. 752–759, Jun. 1999.

[4] L. Li, J. Y. Zhu, and X. M. Chen, "Measurement error of temperature coefficient of resonant frequency for microwave dielectric materials by $TE_{01\delta}$-mode resonant cavity method," *IEEE Trans. Microw. Theory Techn.*, vol. 64, no. 11, pp. 3781–3786, Nov. 2016.

[5] S. N. Dudorov, D. V. Lioubtchenko, J. A. Mallat, and A. V. Raisanen, "Millimeter-wave permittivity measurement of deposited dielectric films using the spherical open resonator," *IEEE Microw. Wireless Compon. Lett.*, vol. 15, no. 9, pp. 564–566, Sep. 2005.

[6] G. Govind and M. J. Akhtar, "Microwave subsurface imaging of dielectric structures using fractal geometries of complementary split ring resonators," *Int. J. RF Microw. Comput.-Aided Eng.*, vol. 29, no. 3, Mar. 2019, Art. no. e21638.

[7] Y. Kato and M. Horibe, "New permittivity measurement methods using resonant phenomena for high-permittivity materials," *IEEE Trans. Instrum. Meas.*, vol. 66, no. 6, pp. 1191–1200, Jun. 2017.

[8] H.-W. Chao and T.-H. Chang, "Wide-range permittivity measurement with a parametric-dependent cavity," *IEEE Trans. Microw. Theory Techn.*, vol. 66, no. 10, pp. 4641–4648, Oct. 2018.

[9] A. Kik, "Complex permittivity measurement using a ridged waveguide cavity and the perturbation method," *IEEE Trans. Microw. Theory Techn.*, vol. 64, no. 11, pp. 3878–3886, Nov. 2016.

[10] K. Y. You, "Materials characterization using microwave waveguide system," in *Microwave Systems and Applications*. Rijeka, Croatia: InTech, 2017, pp. 341–358.

[11] F. Costa *et al.*, "Electromagnetic characterisation of materials by using transmission/reflection (T/R) devices," *Electronics*, vol. 6, no. 4, p. 95, Nov. 2017.

[12] A. M. Nicolson and G. F. Ross, "Measurement of the intrinsic properties of materials by time-domain techniques," *IEEE Trans. Instrum. Meas.*, vol. IM-19, no. 4, pp. 377–382, Nov. 1970.

[13] W. B. Weir, "Automatic measurement of complex dielectric constant and permeability at microwave frequencies," *Proc. IEEE*, vol. 62, no. 1, pp. 33–36, Jan. 1974.

[14] U. C. Hasar, "A microwave method for noniterative constitutive parameters determination of thin low-loss or lossy materials," *IEEE Trans. Microw. Theory Techn.*, vol. 57, no. 6, pp. 1595–1601, Jun. 2009.

[15] I. I. Nefedova, D. V. Lioubtchenko, I. S. Nefedov, and A. V. Raisanen, "Dielectric constant estimation of a carbon nanotube layer on the dielectric rod waveguide at millimeter wavelengths," *IEEE Trans. Microw. Theory Techn.*, vol. 63, no. 10, pp. 3265–3271, Oct. 2015.

[16] P. Deo, D. Mirshekar-Syahkal, L. Seddon, S. E. Day, and F. A. Fernandez, "Microstrip device for broadband (15–65 GHz) measurement of dielectric properties of nematic liquid crystals," *IEEE Trans. Microw. Theory Techn.*, vol. 63, no. 4, pp. 1388–1398, Apr. 2015.

[17] M. D. Janezic, D. F. Williams, V. Blaschke, A. Karamcheti, and C. S. Chang, "Permittivity characterization of low-k thin films from transmission-line measurements," *IEEE Trans. Microw. Theory Techn.*, vol. 51, no. 1, pp. 132–136, Jan. 2003.

[18] C. K. Campbell, "Free-space permittivity measurements on dielectric materials at millimeter wavelengths," *IEEE Trans. Instrum. Meas.*, vol. IM-27, no. 1, pp. 54–58, Mar. 1978.

[19] V. Singh and S. Bhattacharyya, "A free space frequency-time-domain technique for electromagnetic characterization of materials using reflection-based measurement," *Int. J. RF Microw. Comput.-Aided Eng.*, vol. 31, no. 1, Jan. 2021, Art. no. e22490.

[20] S. Sahin, N. K. Nahar, and K. Sertel, "A simplified Nicolson–Ross–Weir method for material characterization using single-port measurements," *IEEE Trans. THz Sci. Technol.*, vol. 10, no. 4, pp. 404–410, Jul. 2020.
[21] Z. Abbas, R. D. Pollard, and R. W. Kelsall, "A rectangular dielectric waveguide technique for determination of permittivity of materials at W-band," *IEEE Trans. Microw. Theory Techn.*, vol. 46, no. 12, pp. 2011–2015, Dec. 1998.
[22] M. W. Hyde and M. J. Havrilla, "A nondestructive technique for determining complex permittivity and permeability of magnetic sheet materials using two flanged rectangular waveguides," *Prog. Electromagn. Res.*, vol. 79, pp. 367–386, 2008.
[23] M. W. Hyde IV, M. I. J. Havrilla, and A. E. Bogle, "Nondestructive determination of the permittivity tensor of a uniaxial material using a two-port clamped coaxial probe," *IEEE Trans. Microw. Theory Techn.*, vol. 64, no. 1, pp. 239–246, Jan. 2016.
[24] R. V. Haro-Báez, J. Córcoles, J. A. Ruiz-Cruz, J. R. Montejo-Garai, and J. M. Rebollar, "Higher-order mode electromagnetic analysis of a material sample between two flanged coaxial probes for broadband modelling of dielectric measurement setups," *Adv. Math. Phys.*, vol. 2019, pp. 1–17, Jan. 2019.
[25] X.-C. Wang, A. Díaz-Rubio, and S. A. Tretyakov, "An accurate method for measuring the sheet impedance of thin conductive films at microwave and millimeter-wave frequencies," *IEEE Trans. Microw. Theory Techn.*, vol. 65, no. 12, pp. 5009–5018, Dec. 2017.
[26] D. M. Pozar, *Microwave Engineering*. Hoboken, NJ, USA: Wiley, 2009.
[27] C. Metaxas and J. L. Driscoll, "A comparison of the dielectric properties of paper and board at microwave and radio frequencies," *J. Microw. Power*, vol. 9, no. 2, pp. 79–89, Jan. 1974.
[28] A. Bisognin *et al.*, "Inkjet coplanar square monopole on flexible substrate for 60-GHz applications," *IEEE Antennas Wireless Propag. Lett.*, vol. 13, pp. 435–438, 2014.
[29] S. Khanal *et al.*, "Towards printed millimeter-wave components: Material characterization," in *Proc. Global Symp. Millim. Waves (GSMM) ESA Workshop Millimetre-Wave Technol. Appl.*, Jun. 2016, pp. 1–3.
[30] *Gorilla Glass 6*, document Rev. 08102020, Corning Technologies, 2020. [Online]. Available: https://www.corning.com/gorillaglass/worldwide/en/glass-types/gorilla-glass-6.html
[31] J. M. Catala-Civera, A. J. Canos, F. L. Penaranda-Foix, and E. D. L. R. Davo, "Accurate determination of the complex permittivity of materials with transmission reflection measurements in partially filled rectangular waveguides," *IEEE Trans. Microw. Theory Techn.*, vol. 51, no. 1, pp. 16–24, Jan. 2003.
[32] *Vector Network Analyzer Uncertainty Calculator*, document Rev. A.05.00.017.0000, Keysight Technologies, 2021. [Online]. Available: https://www.keysight.com/fi/en/lib/software-detail/computer-software/downloadable-vector-network-analyzer-uncertainty-calculator-1000000418epsgsud.html

Xuchen Wang received the B.Sc. degree in optical information science and technology from Northwestern Polytechnical University, Xi'an, China, in 2011, the master's degree from the Department of Optical Engineering, Zhejiang University, Hangzhou, China, in 2014, and the Ph.D. degree (Hons.) from the Department of Electronics and Nanoengineering, School of Electrical Engineering, Aalto University, Aalto, Finland, in 2020.

He worked as a Radio Frequency Engineer in Huawei and TP-Link from 2014 to 2016. He is currently working as a Post-Doctoral Researcher under the supervision of Prof. S. Tretyakov. His main research interests include electromagnetic measurements, space-time metamaterials and metasurfaces, and antennas.

Sergei A. Tretyakov (Fellow, IEEE) received the Dipl. Engineer-Physicist, the Candidate of Sciences (Ph.D.), and the D.Sci. degrees in radiophysics from St. Petersburg State Technical University, Russia, in 1980, 1987, and 1995, respectively.

From 1980 to 2000, he was with the Radiophysics Department, St. Petersburg State Technical University. He is currently a Professor of radio engineering with the Department of Electronics and Nanoengineering, Aalto University, Aalto, Finland. He worked as a Visiting Scientist, CEA-CESTA (French Atomic Energy Commission research center), also affiliated with the University of Bordeaux, Laboratory of Wave-Material Interactions, in 1994, and as a Visiting Professor with the Abbe Center of Photonics, Friedrich Schiller University Jena, Germany (June–July 2013) and at the Department of Photonics Engineering, Technical University of Denmark (January 2013–April 2013). His main scientific interests are electromagnetic field theory, complex media electromagnetics, and microwave engineering. He was the General Chair of the conference series Congress on Advanced Electromagnetic Materials in Microwaves and Optics (Metamaterials) from 2007 to 2014.

Prof. Tretyakov served as a President for the European Virtual Institute for Artificial Electromagnetic Materials and Metamaterials (Metamorphose VI) from 2007 to 2013 and as a Chairperson of the St. Petersburg IEEE ED/MTT/AP Chapter from 1995 to 1998.